catalysts

MDPI

Article

The Catalytic Hydrogenation of Maleic Anhydride on $CeO_{2-\delta}$-Supported Transition Metal Catalysts

Xin Liao [1,2], Yin Zhang [1], Junqiu Guo [2], Lili Zhao [1], Martyn Hill [2], Zheng Jiang [1,2,*] and Yongxiang Zhao [1,*]

1 Engineering Research Center of Ministry of Education for Fine Chemicals, School of Chemistry and Chemical Engineering, Shanxi University, Taiyuan 030006, China; xl19e13@soton.ac.uk (X.L.); sxuzhy@sxu.edu.cn (Y.Z.); lzhao@sxu.edu.cn (L.Z.)

2 Faculty of Engineering and the Environment, University of Southampton, Highfield, Southampton SO17 1BJ, UK; jg10g13@soton.ac.uk (J.G.); M.Hill@soton.ac.uk (M.H.)

* Correspondence: z.jiang@soton.ac.uk (Z.J.); yxzhao@sxu.edu.cn (Y.Z.); Tel.: +44-0-238-059-4893 (Z.J.)

Academic Editor: Leonarda F. Liotta

Received: 11 August 2017; Accepted: 8 September 2017; Published: 14 September 2017

Abstract: The proper selection of transition metals and support is pivotal to the design of active and selective catalysts for maleic anhydride hydrogenation (MAH). Herein, the $M/CeO_{2-\delta}$ (M = Co, Ni, Cu, respectively) catalysts with pre-optimised metal loading of 10 wt % were prepared via a wet impregnation method and well characterized to corroborate their MAH performance with the properties of metal, support and the $M/CeO_{2-\delta}$ catalysts. The results revealed that the metal dispersion on the catalyst declines in the order of $Ni/CeO_{2-\delta}$ > $Co/CeO_{2-\delta}$ > $Cu/CeO_{2-\delta}$, similar to the apparent activity for maleic anhydride (MA) transformation to succinic anhydride (SA). The hydrogenolysis of SA to γ-butyrolactone (GBL) occurs on $Ni/CeO_{2-\delta}$ and $Co/CeO_{2-\delta}$ only when the MA → SA transformation completing. The $Ni/CeO_{2-\delta}$ displays superior activity and selectivity to $Co/CeO_{2-\delta}$ in both MA → SA and SA → GBL reactions, while the $Cu/CeO_{2-\delta}$ and $CeO_{2-\delta}$ are both inert for SA → GBL hydrogenolysis. The MA hydrogenation to SA follows the first order kinetic law on the $Ni/CeO_{2-\delta}$ and $Co/CeO_{2-\delta}$ catalysts yet a more complex kinetic characteristics observed on the $Cu/CeO_{2-\delta}$. The distinct catalytic hydrogenation behaviours of the $M/CeO_{2-\delta}$ catalysts are assigned to the synergism of dispersion and electronic configuration of the transition metals and oxygen vacancies.

Keywords: hydrogenation; maleic anhydride; transition metal catalysts; ceria; oxygen vacancy

1. Introduction

Catalytic hydrogenation of maleic anhydride (MA) is an essential route for the current industrial production of the succinic anhydride (SA), γ-butyrolactone (GBL) and tetrahydrofuran (THF), which are value-added intermediates for pharmaceuticals and bio-degradable polymers and highly-demanded solvents for various industrial processes [1–3]. However, the MA hydrogenation (MAH) is a rather complex process that requires deliberately selecting metal catalyst to avoid excessive hydrogenation and concomitance of ring-open side reaction [1].

Currently, the main catalysts widely applied in the MAH processes are noble metal catalysts (Pd, Ru and Au) [4] and transition metal copper chromite (Cu-Cr) catalysts [5], though they are either costly, less selective or toxic. For developing environmentally-friendly and low-cost alternative MAH catalysts, extensive efforts have been made on: (1) exploring various transition metal Ni [1,2,6], Co [3], Cu [7–9] and bimetallic catalysts [10] with controlled particle sizes and surface dispersion; (2) modifying the traditional porous Al_2O_3 [11], SiO_2 [3], zeolite [2] and SiO_2-Al_2O_3 composite oxide supports [8] using functional promoters (e.g., CeO_2 [12], TiO_2 [13] and ZrO_2 [14], etc.) to moderate the

surface acidity and redox properties [8,15,16]; and (3) employing new catalyst supports, for example the structure-defective TiO_2 [17] and CeO_2 [1] have emerged as excellent supports for metallic Ni catalysts and demonstrated exceptional selectivity in MAH. The previous research advances in MAH catalysts revealed that their activity and selectivity depend greatly on the proper selection of metal and support and on the corresponding metal-support interaction. However, the systematic and comparative studies of the influence of transition metals and their supports on the MAH performance have not been well documented in literature, in particular the emerging ceria and titania supports.

In our previous work, the superior activity and selectivity in MAH on the $Ni/CeO_{2-\delta}$ catalyst to those on the Ni/Al_2O_3 catalyst was attributed to the synergism of the Ni-$CeO_{2-\delta}$ interaction, the oxygen vacancies and developed porosity of the $CeO_{2-\delta}$ support [1]. In theory, the electron-rich O_{vac} in $CeO_{2-\delta}$ may modify the geometric and electronic structure of the active metal [18,19], as well as enforce the metal-support interaction [20]. It is thought that the O_{vac} defects could synergistically enhance the catalytic performance of $M/CeO_{2-\delta}$ catalysts, through coordination with the oxygen-containing group in OH cleavage [21], NO_2 reduction [22] and CO_2 methanation [23]. Moreover, the ionic TM ($M^{\delta+}$) species can diffuse into the CeO_2 lattice and modulate the population of O_{vac} in mixed oxides with dependence of the ionic radius and the valence state of the M [24,25]. Although $M/CeO_{2-\delta}$ catalysts have been examined in various catalytic reactions, there is very limited knowledge of the metal influences on the $CeO_{2-\delta}$ supports, particularly for the activity and selectivity in MAH.

In this paper, various TMs (Co, Ni, Cu) supported on ceria were prepared by a simple wet impregnation method and employed in liquid phase hydrogenation of MA at 210 °C and 5 MPa. Through careful characterizations, the catalyst activity and product selectivity in MAH on the $M/CeO_{2-\delta}$ were investigated and correlated to the properties of the materials.

2. Results and Discussion

2.1. Structure and Morphology

Figure 1A shows the powder X-ray diffraction (XRD) data of CeO_2 and MO_x/CeO_2 (M = Co, Ni, Cu, respectively) precursors. For the CeO_2 and MO_x/CeO_2 samples, the major Bragg diffraction peaks at 28.5°, 33.1° and 47.5° are clearly resolved and attributed to the diffractions from the (111), (200) and (220) planes of the cubic fluorite-type ceria (JCPDS file 34-0394), respectively. The weak diffraction peaks are associated with isolated metal oxides and indexed to CuO (JCPDS file 48-1548), NiO (JCPDS file 78-0643) and Co_3O_4 (JCPDS file 43-1003) (Figure 1A). The diffraction peaks of CeO_2 in the MO_x/CeO_2 catalysts slightly shift to greater 2θ angles than those of bare CeO_2, revealing that small portions of the $M^{+\delta}$ ions in the loaded MO_x have diffused into the ceria matrix and partially substituted cerium cations (radius of Ce^{4+} = 0.084 nm) [1,25,26]. Indeed, the metal doping induces lattice distortion and shrinkage of the CeO_2 lattice to different levels (Table 1) due to the smaller radii of the doping cations (R(Co^{2+}) = 0.074 nm and R(Co^{3+}) = 0.063 nm, R(Ni^{2+}) = 0.072 nm and R(Cu^{2+}) = 0.073 nm), but the changes of lattice parameters of CeO_2 for the samples are insignificant because of the low doping level.

The calculated mean crystalline sizes of Co_3O_4, NiO, CuO and CeO_2 are listed in Table 1. It is found that NiO possesses the smallest crystallite size, while CuO the largest. The CeO_2 supports exhibit different crystallite sizes even though the MO_x are loaded at similar amounts. The varying crystallite sizes of MO_x and CeO_2 are due to their different MO_x-CeO_2 interaction and the induced lattice distortion.

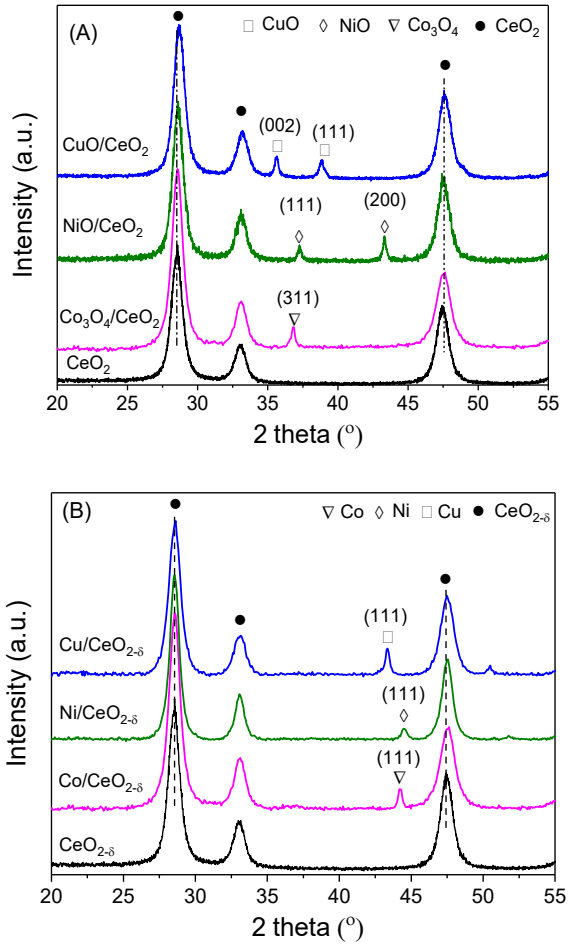

Figure 1. XRD pattern of (**A**) the MO_x/CeO_2 precursors and (**B**) the $M/CeO_{2-\delta}$ catalysts (M = Co, Ni, Cu, respectively).

Table 1. The properties of the MO_x/CeO_2 precursors and corresponding $M/CeO_{2-\delta}$ catalysts.

Sample	a(CeO_2) (nm)	a($CeO_{2-\delta}$) (nm)	Loading (wt %)	Crystallite Size (nm)			
				D(CeO_2)	D($CeO_{2-\delta}$)	D(MO_x)	D(M)
CeO_2	0.5438	0.5438	-	12.5	12.9	-	-
$Co/CeO_{2-\delta}$	0.5430	0.5442	10.3	14.3	15.2	15.7	12.8
$Ni/CeO_{2-\delta}$	0.5424	0.5441	9.8	12.5	16.5	13.2	9.8
$Cu/CeO_{2-\delta}$	0.5413	0.5442	9.7	13.2	15.7	16.7	13.4

Note: a(CeO_2) and a($CeO_{2-\delta}$) denote the lattice parameter of CeO_2 in the MO_x/CeO_2 and reduced $M/CeO_{2-\delta}$, respectively, calculated using interplanar distance (d) and Miller indices (*h k l*) in the equation $a = d \times \sqrt{h^2 + k^2 + l^2}$. Metal loading amount was determined by ICP-OES. D(CeO_2) and D($CeO_{2-\delta}$) are the crystalline size of CeO_2 in the MO_x/CeO_2 and $M/CeO_{2-\delta}$; D(MO_x) and D(M) denote the crystallite size of metal oxide and metal calculated using the Scherrer equation.

After H_2 reduction treatments, metal phases of Ni, Co and Cu emerge in the XRD patterns of the reduced $M/CeO_{2-\delta}$ catalysts (Figure 1B), while the MO_x diffraction peaks vanish since the crystalline MO_x species are converted to corresponding metals. Compared to Co and Cu, the Ni species display relatively weaker diffraction, suggesting that Ni might be highly dispersed on the surface of $CeO_{2-\delta}$ with a smaller crystallite size (Table 1). We suppose that the smaller crystallite sizes of metals relative to their metal oxides (Figure 2) are induced by the H_2 reduction treatment because the M-$CeO_{2-\delta}$ would inherit the strong interaction between MO_x and the CeO_2. The proportional reliance of metal crystallite sizes on their corresponding metal oxides is further confirmed by the crystallite size changes

of $Ni/CeO_{2-\delta}$ and NiO/CeO_2 samples (Figure S1 in Supplementary Materials), where the strong dependence of the Ni^0 crystallite sizes on their oxide precursors showed a linear correlation with the Ni loading up to 20 wt %.

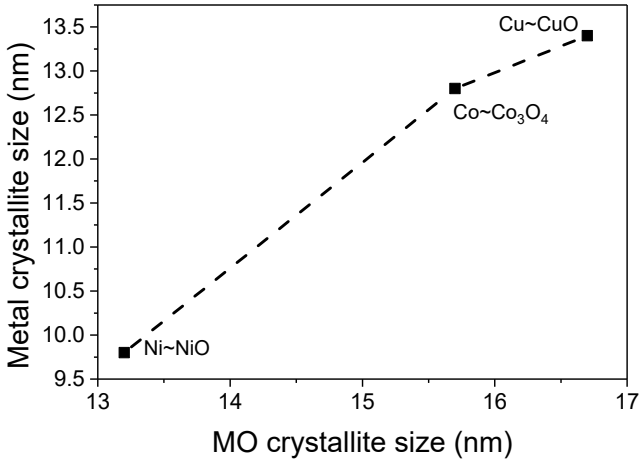

Figure 2. The dependence of metal crystallite sizes on those of metal oxides.

As shown in Table 1, the lattice parameters of ceria in the $M/CeO_{2-\delta}$ catalysts appear quite similar, but become larger than those of MO_x/CeO_2 samples. The increasing crystallite sizes of ceria in $M/CeO_{2-\delta}$ catalysts may be induced by comprehensive factors, including a fraction of Ce^{4+} cations being reduced to Ce^{3+} of a larger ionic radius ($R_{Ce(III)}$ = 0.102 nm [27]) that expands the ceria lattice parameter, the thermal sintering of ceria and the metal exiting from ceria matrices during the reduction process.

Figure 3 shows the transition electron microscopy (TEM) images of reduced the $M/CeO_{2-\delta}$ catalysts. It is found that most CeO_2 crystallites observed in the $M/CeO_{2-\delta}$ samples are of spherical or irregular polyhedral morphologies, independent of the deposited metals. From the TEM images, it is difficult to distinguish the metal particles because the sizes of metals are quite similar to the CeO_2 support (shown in Table 1) [25]. In addition, a larger $CeO_{2-\delta}$ particle is seen in the $Co/CeO_{2-\delta}$ catalyst compared with $Ni/CeO_{2-\delta}$ and $Cu/CeO_{2-\delta}$, which is likely associated with the slight sintering of the ceria support during the reduction at higher temperature.

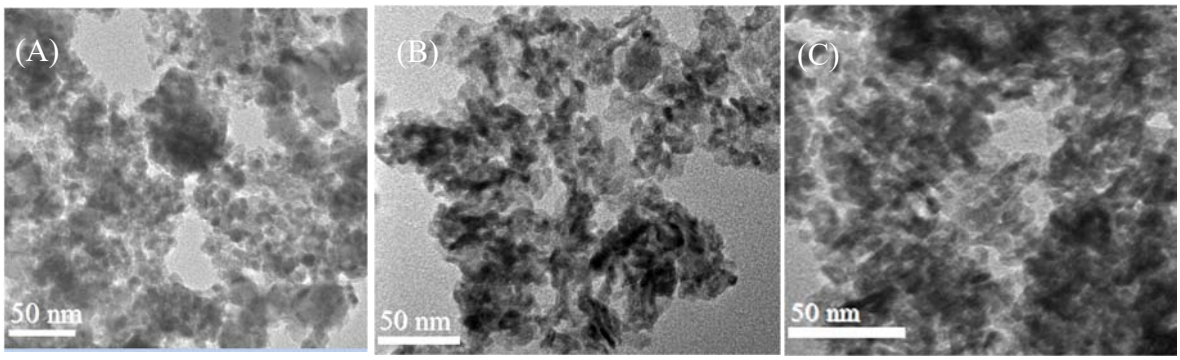

Figure 3. TEM images of $M/CeO_{2-\delta}$ samples. (**A**) $Co/CeO_{2-\delta}$; (**B**) $Ni/CeO_{2-\delta}$ and (**C**) $Cu/CeO_{2-\delta}$.

2.2. Reduction Behaviour of the MO_x/CeO_2 Catalyst Precursors

Figure 4 shows the hydrogen temperature-programmed reduction (H_2-TPR) profiles of MO/CeO_2 samples. The TPR profiles at the temperature below 400 °C are due to the reduction of supported MO_x in the three MO_x/CeO_2 samples. For the CuO/CeO_2 sample, the strong peak centred at 160 °C is

attributed to the reduction of isolated CuO species with weak CuO-CeO_2 interaction, while the shoulder peak located at 130 °C is due to the reduction of adsorbed O species on O_{vac} sites and the highly dispersed CuO with strong CuO-CeO_2 interaction [26]. For the NiO/CeO_2 sample, the reduction of surface adsorbed O species starts from an even lower temperature (~100 °C) [28] with a sharp reduction peak at 195 °C, which can be related to the reduction of highly dispersed NiO on CeO_2 [28]. The main TPR peak at 260 °C is assigned to the reduction of NiO clusters aggregated on the CeO_2 surface [1]. On the Co_3O_4/CeO_2 sample, three distinct TPR peaks are observed, which could be ascribed to the reductions of Co_3O_4 → CoO (220 °C), CoO → Co (270 °C) [29,30] and isolated CoO species (380 °C), respectively [25]. It is worth noting that the CeO_2 reduction occurs at a lower temperature for Co_3O_4/CeO_2 relative to other samples, because CoO_x can enhance H_2 spillover from the reduced Co species towards CeO_2, which decreases the CeO_2 reduction temperature [31]. The different interaction between the MO_x and CeO_2, as indicated by their distinct reduction behaviours of the MO_x/CeO_2 samples, would determine the dispersion of the corresponding metals on $CeO_{2-\delta}$ and thus affect their ability in hydrogen activation (see Section 2.4 for the H_2-TPD analysis).

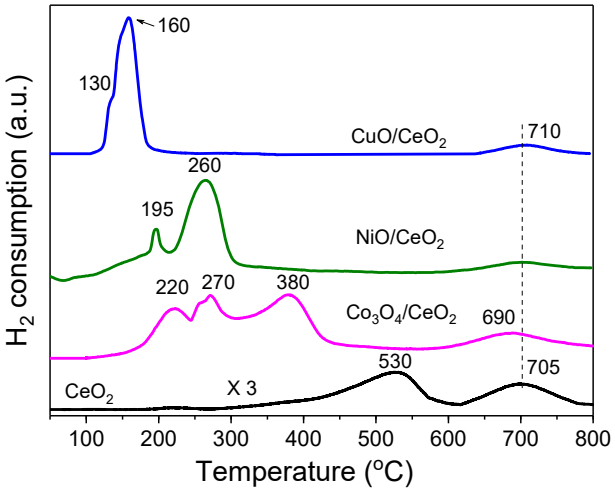

Figure 4. The H_2-temperature-programmed reduction (TPR) profiles of MO_x/CeO_2 samples.

The two broad reduction peaks appearing at 530 and 705 °C for CeO_2 are attributed to the respective reductions of surface oxygen species and the bulk lattice oxygen within ceria [32]. However, for the three MO_x/CeO_2 samples, their reduction peaks due to the removal of lattice oxygen from the CeO_2 support are displayed in a similar temperature region (600~800 °C), suggesting that the involved MO_x species slightly impact the reducibility of the lattice oxygen of CeO_2. In contrast, the reduction of surface oxygen (~530 °C) is absent for the MO_x/CeO_2 since both the strong M-ceria interaction and the H_2 spillover from metal onto the vicinity surface oxygen species can improve the surface oxygen removal from the CeO_2 support [33]. In other words, the metal on the support can catalyse the ceria reduction.

2.3. Surface Structural Analysis

Raman spectroscopy is employed to investigate the surface structure of the MO_x/CeO_2 precursors and the M/$CeO_{2-\delta}$ catalysts. As shown in Figure 5A, the strong vibration mode (F_{2g}, ~466 cm^{-1}), due to the symmetrical stretching vibration of Ce-O bonds, dominates the Raman spectrum of CeO_2 [34]. Upon metal loading, the F_{2g} modes red shift to 454 cm^{-1} with peak broadening due to the strong interaction between MO_x and CeO_2 that gives rise to distortion of the $CeO_{2-\delta}$ lattice and creates electron-rich O_{vac} for maintaining the system charge neutrality [34]. Besides the F_{2g} band, two broadening bands within the 600~700 cm^{-1} and 1100~1250 cm^{-1} regions are observed on the MO_x/CeO_2 samples, which can be attributed to the Frenkel defect-induced modes (D band) and the

second order longitudinal optical mode (2LO), respectively [35]. The D and 2LO bands are related to the O_{vac} that originated from reducing Ce^{4+} to Ce^{3+}. Compared to CeO_2, MO_x/CeO_2 samples show broader and stronger vibrations in the D bands and 2LO modes, suggesting that the loading of MO_x species facilitates the creation of O_{vac} thanks to metal substitution of lattice Ce, which is in good agreement with the discussion of XRD results. The quasi density of O_{vac} in ceria due to metal incorporation is tentatively quantified through the relative ratio of $(I_D + I_{2LO})/I_{F2g}$, as inserted in Figure 5A. The $(I_D + I_{2LO})/I_{F2g}$ in the MO_x/CeO_2 samples is more than three-fold that in bare CeO_2, namely, the O_{vac} density descends in the order of $NiO/CeO_2 > CuO/CeO_2 > Co_3O_4/CeO_2 >> CeO_2$. The results clearly reflect that the O_{vac} concentration created by the MO_x loading highly depends on the metal species, likely due to their different ionic radius and the oxidation state of the dopants [24].

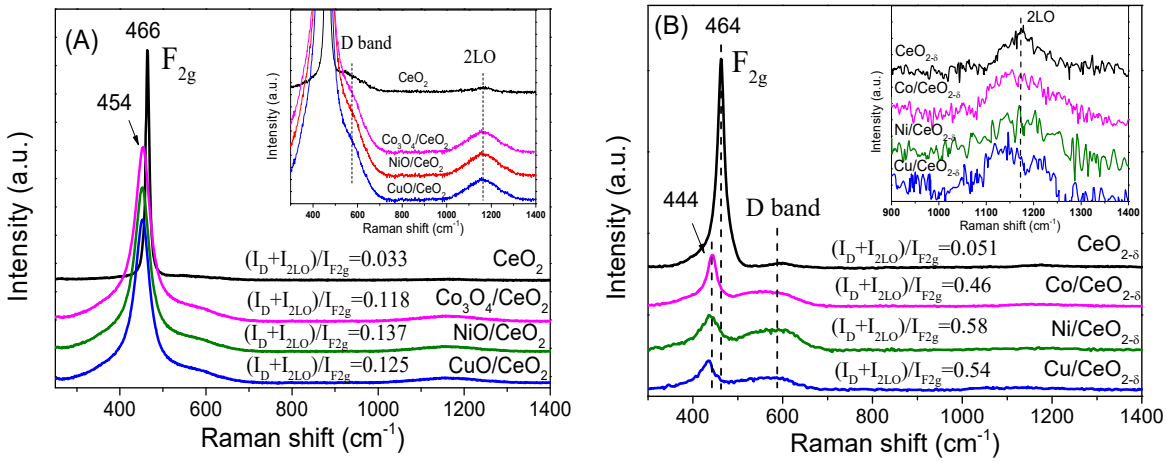

Figure 5. Raman spectra of the MO_x/CeO_2 precursors (**A**) and the reduced $M/CeO_{2-\delta}$ catalysts (**B**). The inserted zoom-in figures underline the existence of 2LO bands.

The modes of F_{2g}, D band and 2LO can be clearly identified in the reduced $M/CeO_{2-\delta}$ catalysts and $CeO_{2-\delta}$ (Figure 5B) but much weaker than those of the MO_x/CeO_2 precursors, in particular the O_{vac}-related D and 2LO bands. Moreover, the F_{2g} modes of $M/CeO_{2-\delta}$ catalysts further red shift from 454 cm^{-1} to 444 cm^{-1}. The relative changes of Raman signals for the $M/CeO_{2-\delta}$ catalysts to their precursors are the consequence of their decreased structure symmetry. However, the $(I_D + I_{2LO})/I_{F2g}$ ratios of the $M/CeO_{2-\delta}$ catalysts and $CeO_{2-\delta}$ are much greater than those in their corresponding oxides (inserted in Figure 5A,B), suggesting that the H_2 reduction significantly promotes O_{vac} density. It is worth noting that O_{vac} concentration of the metal-loaded catalysts is enhanced approximately nine- to ten-fold that of $CeO_{2-\delta}$, further confirming that metal loading can dramatically improve the O_{vac} formation. The results are in good accordance with the TPR characterization. We also note that the O_{vac} density variation of the $M/CeO_{2-\delta}$ catalysts follows the descending order of $Ni/CeO_{2-\delta} > Cu/CeO_{2-\delta} > Co/CeO_{2-\delta} >> CeO_{2-\delta}$, which inherits the O_{vac} concentration order of their precursor oxides.

2.4. Hydrogen Activation on the $M/CeO_{2-\delta}$ Catalysts

Hydrogen temperature programmed desorption (H_2-TPD) is a powerful tool to gain insights into hydrogen activation and metal-support interaction on the catalysts. As shown in Figure 6, the H_2-TPD profiles of the $M/CeO_{2-\delta}$ are deconvoluted into three peaks. The α peaks for the $M/CeO_{2-\delta}$ catalysts appear within a very similar temperature region, which is identical to the temperature range of the sole H_2-TPD peak on $CeO_{2-\delta}$. Such α peaks are therefore assigned to the desorption of H_2 up-taking surface O_{vac} sites in $CeO_{2-\delta}$ [27]. The difference in the integrated areas (Table 2) reveals that the amount of O_{vac} of the $M/CeO_{2-\delta}$ is dependent on the metallic species, and the $Ni/CeO_{2-\delta}$ and

$Cu/CeO_{2-\delta}$ possess a similar amount of O_{vac}, but much larger than those of the $Co/CeO_{2-\delta}$ and $CeO_{2-\delta}$ supports. The results are consistent with the Raman and TPR analyses.

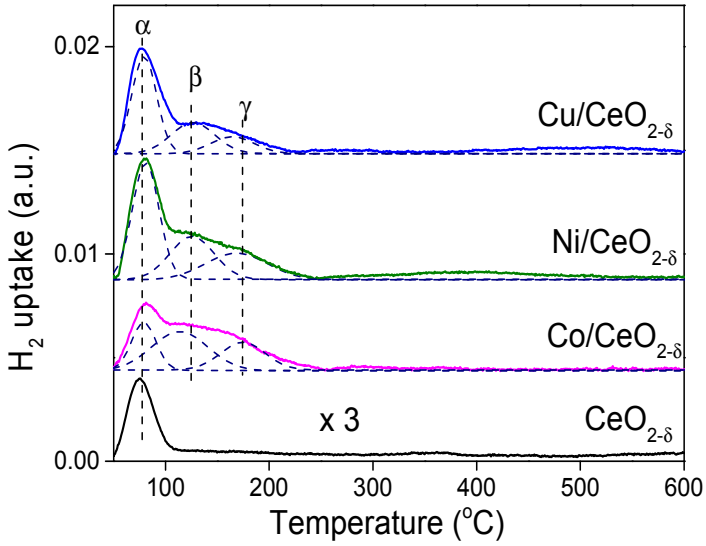

Figure 6. H_2 temperature programmed desorption (TPD) profiles of $CeO_{2-\delta}$ and $M/CeO_{2-\delta}$ catalysts.

Table 2. H_2 uptake, metal dispersion and hydrogenation rate constants on the $M/CeO_{2-\delta}$ catalyst.

Sample	H_α (μmol/g)	H_β (μmol/g)	H_γ (μmol/g)	$\Sigma(H_\beta + H_\gamma)$ (μmol/g)	ΣH (μmol/g)	D_M (%)	Rate Coefficient, k (min^{-1})
$Co/CeO_{2-\delta}$	17.28	24.04	11.84	35.9	53.16	3.9	0.0588
$Ni/CeO_{2-\delta}$	28.35	22.6	14.6	37.2	65.55	4.4	0.0216
$Cu/CeO_{2-\delta}$	28.74	14.2	8.2	22.4	52.14	2.9	-
$CeO_{2-\delta}$	7.87	/	/	/	7.87	/	0.0037

Note: D_M denotes the metal dispersion, calculated via $D_M = (M_{surf}/M_{total})$, where M_{surf} and M_{total} are the amount of surface-exposed metal and total metal loading, respectively. Assuming H/M = 1 and $M_{surf} = 2 \times$ (H_2 desorption from metal surface), M_{surf} can be calculated from the amount of hydrogen (β and γ peaks) uptaken on the metal [1].

The β and γ peaks located in 100–250 °C are due to H_2 desorption from the corresponding metal species. The β peaks can be ascribed to the dissociative H_2 adsorbed on the highly dispersed metal species with a large density of surface defects, which can enhance the hydrogen diffusion and reduce the energy barrier for hydrogen dissociation [36]. The γ peaks are associated with chemisorbed hydrogen on isolated metal clusters [37]. The quantitative analyses of peak β and γ (Table 2) clearly show that $Co/CeO_{2-\delta}$ and $Ni/CeO_{2-\delta}$ catalysts possess comparable amounts of β-H_2 and γ-H_2, which are more than those of $Cu/CeO_{2-\delta}$. The low uptake of β and γ hydrogen on $Cu/CeO_{2-\delta}$ may be due to the weak capability of Cu for hydrogen activation caused by its closed d^{10} orbitals [38].

According to the assignment of the H_2-TPD peaks, the metal dispersion (D_M) can be quantified using only the metal-related hydrogen activation (sum of the β- and γ-H_2), which is different from the overall H_2 activation amount of the catalysts. As listed in Table 2. The D_M of the $M/CeO_{2-\delta}$ catalysts is found to be decreasing in the order of $Ni/CeO_{2-\delta} > Co/CeO_{2-\delta} > Cu/CeO_{2-\delta}$.

2.5. Catalytic Hydrogenation of Maleic Anhydride

Figure 7A presents the MA conversion (X_{MA}) along the hydrogenation courses on $M/CeO_{2-\delta}$ catalysts in a batch reactor at 210 °C and hydrogen pressure of 5.0 MPa. Among the examined catalysts, $Ni/CeO_{2-\delta}$ is found to possess the highest activity of MA conversion, reaching ~100% MA conversion in 60 min. However, the MA conversion on $Cu/CeO_{2-\delta}$ and $Co/CeO_{2-\delta}$ in the same period only achieves 32% and 70%, respectively. The MA transformation completes in 3 h on $Co/CeO_{2-\delta}$ and

4 h on $Cu/CeO_{2-\delta}$. Moreover, the turnover frequencies of MA transformed to SA ($TOF_{MA\rightarrow SA}$) over $M/CeO_{2-\delta}$ catalysts are also estimated. The $Ni/CeO_{2-\delta}$ catalyst records the highest $TOF_{MA\rightarrow SA}$ of 61.7 min^{-1}, nearly twice that of the $Co/CeO_{2-\delta}$ catalyst ($TOF_{MA\rightarrow SA}$ = 31.2 min^{-1}) and five-fold that of $Cu/CeO_{2-\delta}$ ($TOF_{MA\rightarrow SA}$ = 13.2 min^{-1}). The considerable difference of the MA conversion on the $M/CeO_{2-\delta}$ catalysts cannot only be attributed to the particle size or metal dispersion effects because the activity difference is much more significant. We speculate that there exist other factors, such as the intrinsic properties (e.g., electronic configuration) of individual metals, M-support interaction and O_{vac} amount, to influence the catalytic performance synergistically.

Figure 7B presents the curves of $-\ln(1 - X_{MA})$ versus time within the first 60 min, which are fitted according to the first order kinetic law in terms of MA conversion on the metal-based catalysts [17]. The linear kinetic plots over $Ni/CeO_{2-\delta}$ and $Co/CeO_{2-\delta}$ catalysts suggest that the C=C hydrogenation follows the quasi-first order reaction in terms of MA conversion, while the nonlinear kinetic plot on $Cu/CeO_{2-\delta}$ reflects that its initial hydrogenation follows a complicated kinetic mechanism. The MA hydrogenation rate coefficients (k_1) on the $Ni/CeO_{2-\delta}$ and $Co/CeO_{2-\delta}$ catalysts are determined according to the gradients of their linear plots and summarised in Table 2. The k for $Ni/CeO_{2-\delta}$ is much greater than that for $Co/CeO_{2-\delta}$, indicating that metallic $Ni/CeO_{2-\delta}$ is more reactive than $Co/CeO_{2-\delta}$.

In principle, the electronic configurations of the active metals are profound in the activation of MA for the hydrogenation reaction. The previous DFT simulation demonstrated that the adsorption and activation of MA on the metal surface are primarily controlled by the back-donation of the electron from the metal onto the anti-bonding π^* orbital of maleic anhydride [39]. Therefore, the metallic Cu with a full-filled $3d^{10}$ electronic configuration without the unpaired electron possesses weaker capability of electron-donation to the MA molecule. In contrast, the unpaired electrons of Co ($3d^7$) and Ni (Ni $3d^8$) would favour the coordination and activation of MA, thus exhibit much higher activity.

Besides the intrinsic properties, the O_{vac} is regarded as another factor to enhance the C=C hydrogenation because the O_{vac} can enrich the electron density of active metals, which promotes the electron-donating ability and promotes H_2 dissociation [1,40]. In our cases, the $Ni/CeO_{2-\delta}$ catalyst has richer O_{vac} and, thus, may donate more electrons to metallic Ni in comparison to $Co/CeO_{2-\delta}$. Further, the smaller particle size of Ni (XRD section) also strengthens the short-range electron transferring from O_{vac} onto the adjacent metal clusters. Hence, the abundant O_{vac} and the direct or indirect $O_{vac} \rightarrow M$ electronic donation are responsible for the fact that $Ni/CeO_{2-\delta}$ shows higher activity in MA hydrogenation than $Co/CeO_{2-\delta}$. However, it is noted that $Ni/CeO_{2-\delta}$ and $Cu/CeO_{2-\delta}$ catalysts have a similar O_{vac} amount, but different activity in MA hydrogenation, suggesting that the intrinsic electron structure of active metal dominates the MA hydrogenation.

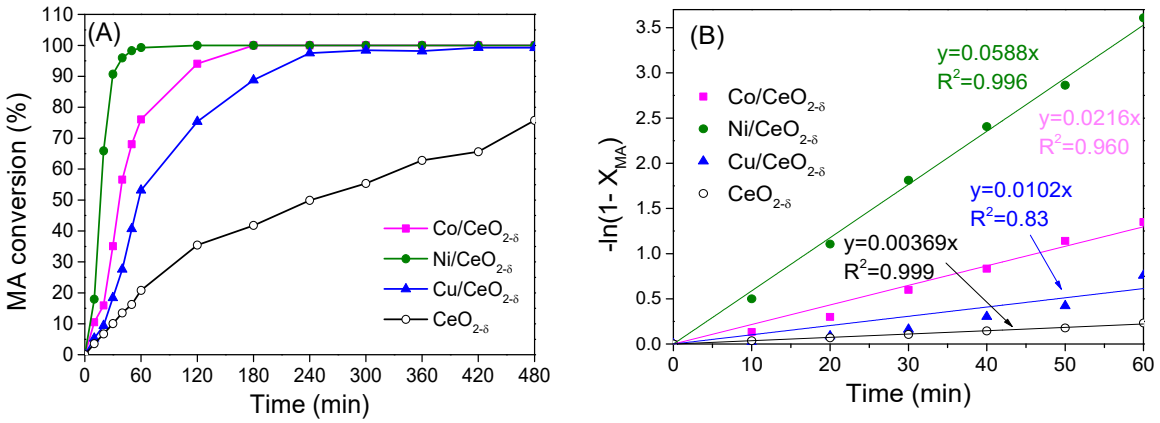

Figure 7. (**A**) The conversion of maleic anhydride (MA) and (**B**) the kinetic curves of the $M/CeO_{2-\delta}$ catalysts.

Figure 8A shows the SA selectivity of the $M/CeO_{2-\delta}$ catalysts in the prolonged MAH for 8 h. The $Cu/CeO_{2-\delta}$ and $CeO_{2-\delta}$ catalysts exhibit 100% selectivity to SA in the 8-h continuous MAH, without GBL observed in the products, indicating they are inert for SA hydrogenolysis to GBL. The $TOF_{SA\rightarrow GBL}$ values over $Ni/CeO_{2-\delta}$, $Co/CeO_{2-\delta}$ and $Cu/CeO_{2-\delta}$ are 3.08 min^{-1}, 0.87 min^{-1} and 0, respectively, indicating that $Ni/CeO_{2-\delta}$ shows the highest activity in the SA → GBL transformation. It is worth noting that GBL was generated only if MA fully converts to SA on the $Ni/CeO_{2-\delta}$, as evidenced by the SA selectivity over $Ni/CeO_{2-\delta}$, which remains 100% in the initial 40 min MAH time-on-stream before declining due to the following GBL generation. The generation of GBL on $Co/CeO_{2-\delta}$ also commences while the conversion of MA to SA is completing. GBL yields (Figure 8B) reach ~25% on $Ni/CeO_{2-\delta}$ and ~5% on $Co/CeO_{2-\delta}$ in 6 h, which are much slower than the MA → SA transformation. The results suggest that MAH on the $M/CeO_{2-\delta}$ is a multiple-step process: MAH to SA occurs first and rapidly, while GBL generates from the hydrogenolysis of SA only if no MA exists in the system. A similar phenomenon has been observed on the TiO_2-supported Ni-based catalysts by Torres et al. [17].

Owing to the complexity of the MAH reaction, its hydrogenation mechanism has not been explicated in the literature, in particular for the $M/CeO_{2-\delta}$ systems, although the theoretical and experimental understanding of H_2 adsorption, activation and cycling on CeO_2 and noble metals was attempted for a variety of redox reactions [38,41]. Even fewer investigations of MA adsorption and hydrogenation over noble metals are openly accessible [39,42]. However, on the basis of our experimental characterization data and the reported fundamental data regarding MAH reaction thermodynamics and kinetics, we may explicitly rationalize the stepwise MAH with a distinct reaction rate and selectivity on the $M/CeO_{2-\delta}$ catalyst systems.

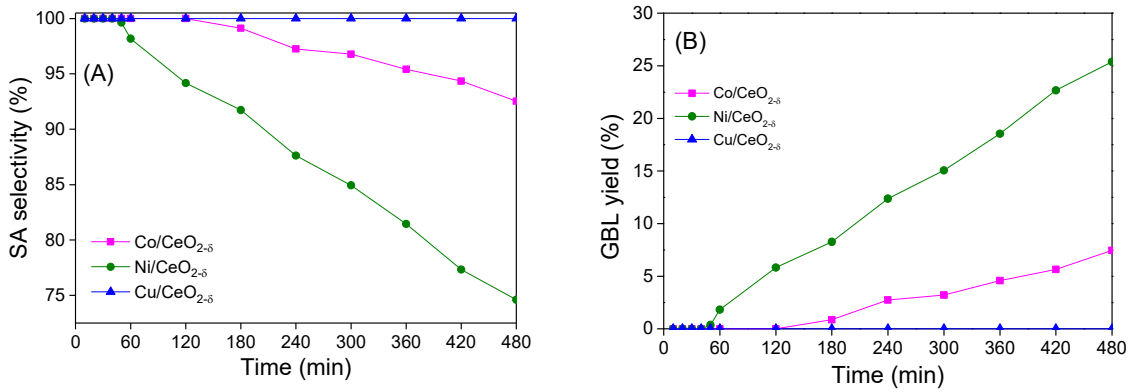

Figure 8. (**A**) The selectivity of succinic anhydride (SA) and (**B**) the yield of γ-butyrolactone (GBL) over $M/CeO_{2-\delta}$ catalysts in the 8 h time.

The preferential hydrogenation of C=C bonds rather than C=O groups in the initial MAH stage can be implicitly interpreted from kinetics and thermodynamic perspectives. The possible reaction routes for MAH to SA and GBL can be written as:

$$MA + H_2 = SA\ \Delta H_{MA\rightarrow SA} = -133.8\ kJ/mol \quad (1)$$

$$SA + 2H_2 = GBL + H_2O\ \Delta H_{SA\rightarrow GBL} = -108.7\ kJ/mol \quad (2)$$

$$MA + 3H_2 = GBL + H_2O\ \Delta H_{MA\rightarrow GBL} = -241.7\ kJ/mol \quad (3)$$

Here, the free enthalpy change data of $\Delta H_{MA\rightarrow SA}$ and $\Delta H_{SA\rightarrow GBL}$ are adopted from the literature [43], while the $\Delta H_{MA\rightarrow GBL}$ of Global Reaction (3) is calculated applying Hess's law to Reactions (1) and (2). Since the molecule kinetic characteristics determine the rate and selectivity, the MA → SA transformation would be more favourable and faster than the SA → GBL and MA → GBL

transformations that involve more H_2 molecules than the former reaction. This interpretation is well evidenced by the fact that the GBL generation initiates only if complete MA → SA transformation on the $M/CeO_{2-\delta}$ catalyst systems occurs, which also reveals that Reaction (3) is least viable on all of the catalysts investigated. Indeed, it was claimed that the C=C group is kinetically more active than the C=O group [44].

As for the distinct selectivity of the chosen $M/CeO_{2-\delta}$ systems, we suppose that their different surface electron configurations of the catalysts, particularly the metal d orbitals, play essential roles, because the overall hydrogenation reaction is usually determined by H_2 activation on the catalysts [42,45]. This argument is also evidenced by our TPD data (Figure 6 and Table 2) where the $Cu/CeO_{2-\delta}$ displays a smaller amount of β and γ hydrogen, namely the weaker ability to activate hydrogen. For the transformation of SA → GBL, the adsorption of the C=O group was also considered to be of profound importance for the hydrogenolysis process [46]. The closed d^{10} shell of metal Cu is not beneficial to C=O hydrogenolysis due to its low interstitial electron density and weak energy for adsorption and activation of the C=O group [47]. In contrast, metallic Ni and Co with partially filled d-orbitals are prone to coordinate with the C=O groups of organic adsorbates and thus facilitate C=O hydrogenolysis [47].

The beneficial contributions of O_{vac} in C=O hydrogenolysis have been widely accepted [48,49]. The O_{vac} in the non-stoichiometric oxides, such as ZnO_{1-x} [50] and CeO_{2-x} [1], can polarise and activate the C=O group and thus reduce the energy barrier of C=O conversion to display reasonable hydrogenolysis selectivity. In this work, the amount of O_{vac} of the $Ni/CeO_{2-\delta}$ catalyst is about 1.5-times that in the $Co/CeO_{2-\delta}$ catalyst, suggesting that $Ni/CeO_{2-\delta}$ catalyst can offer more active sites for C=O activation. However, the calculated $TOF_{SA\rightarrow GBL}$ of $Ni/CeO_{2-\delta}$ is nearly triple that of $Co/CeO_{2-\delta}$, which is larger than the relative O_{vac} ratio between the two catalysts. Therefore, the electronic configuration of the active metal is the key factor to determine the catalytic hydrogenolysis of SA to GBL, while O_{vac} can facilitate C=O conversion on $Ni/CeO_{2-\delta}$ due to the electron-donating and selective adsorption effects.

3. Materials and Methods

All chemical reagents, $Ce(NO_3)_3{\cdot}6H_2O$, $Ni(NO_3)_2{\cdot}6H_2O$, $Cu(NO_3)_2{\cdot}3H_2O$, $Co(NO_3)_2{\cdot}6H_2O$ and citric acid (CA). purchased from the Sinopharm Chemical Reagent Co., Ltd. (Shanghai, China), were analytic grade and used as-purchased without pre-purification.

3.1. Ceria Support Preparation

Ceria supports were prepared by the sol-gel process. First, 5.00 g $Ce(NO_3)_3{\cdot}6H_2O$ were dissolved in 20 mL deionized water containing 6.56 g CA under rigorous stirring. The solution was heated in a water bath at 80 °C until a porous dry gel was obtained. During this process, the colourless solution became light yellow and finally brown. The obtained gel was then dried at 120 °C for 8 h to form a spongy material, which is subject to calcination for 3 h at 500 °C with a heating ramp of 3 °C/min. The resulting cerium oxide was used as the support to prepare the corresponding catalysts.

3.2. $M/CeO_{2-\delta}$ (M = Co, Ni and Cu) Catalysts Preparation

The $M/CeO_{2-\delta}$ (M = Co, Ni, Cu) catalysts (metal loading = 10 wt %) were prepared by an incipient wetness impregnation method as reported in our previous research paper [1]. For the preparation of the $Ni/CeO_{2-\delta}$ catalyst, 1.01 g $Ni(NO_3)_2{\cdot}6H_2O$ were dissolved in 10 mL of the ethanol/DI water (1:1 volumetric ratio) solution, and then, 2.00 g of CeO_2 support were added into the mixed solution. The mixed solution was heated on a hotplate at 80 °C under rigorous stirring to evaporate the solvent before drying at 120 °C for 8 h in a convection oven. The obtained sample was calcined at 450 °C for 3 h in a muffle furnace with the heating ramp of 3 °C/min. The received oxide sample was reduced at 350 °C (heating ramp of 2 °C/min) in H_2 flow for 3 h to obtain the $Ni/CeO_{2-\delta}$ catalyst for MA hydrogenation. The $Cu/CeO_{2-\delta}$ and $Co/CeO_{2-\delta}$ catalysts were prepared using a similar procedure,

but $Cu/CeO_{2-\delta}$ and $Co/CeO_{2-\delta}$ were reduced at 250 °C and 450 °C, respectively, which ensured that all of the transition metal species fully reduced at the optimum temperature as determined by H_2-TPR.

3.3. Catalyst Characterizations

X-ray diffraction data were acquired by powder X-ray diffraction using a D8 Advance (Bruker, Billerica, MA, USA) (Cu $K_{\alpha 1}$ radiation, λ = 0.15418 nm) equipped with a Vantec detector and Ni filter. Data were collected between 10° and 80° 2θ degrees via a continuous scan mode with a scanning rate at 4°/min. The mean crystallite size oof the pertinent species were calculated employing the Scherrer equation: $D = k\lambda/(\beta cos\theta)$, where k is 0.9, β is the full width of the diffraction line at half of the miximum intensity and θ is the diffraction angle. The Ni loading of the catalysts was carried out by means of inductively-coupled plasma (ICP) spectroscopy with the iCAP 7400 ICP-OES (Thermo Fisher Scientific, Waltham, MA, USA) equipment. The Raman spectrum was recorded on a LabRAM HR Evolution Raman microscope with a laser wavelength of 532 nm (HORIBA, Tokyo, Japan) for surface characterization. The morphology of the materials was visualized using a JEOL JEM-2010 transmission electron microscope (TEM) (JEOL, Tokyo, Japan) operated at 120.0 kV. The samples were dispersed in ethanol assisted by the ultrasonic technique.

Hydrogen-temperature programed reduction (H_2-TPR) experiments were performed using the Micromeritics AutoChem II 2950 system (Norcross, GA, USA) equipped with a thermal conductivity detector (TCD). Typically, 30 mg of catalyst were first degassed at 300 °C for 1 h with argon flushing. After cooling down to ambient temperature in argon, H_2/Ar (10 vol % H_2) at a flow rate of 50 mL/min was passed through the catalysts, and the TPR profiles were recorded from 50 to 800 °C at a ramp of 10 °C/min. The output signal of the gas mixture was measured continuously using the TCD as a function of temperature.

Hydrogen temperature programmed desorption (H_2-TPD) measurements were carried out on the same apparatus as TPR. In the H_2-TPD test, 100 mg catalyst were first reduced in situ at 350 °C for 1 h in pure H_2, followed by purging with Ar for 1 h at 360 °C to remove the excess hydrogen adsorbed on the surface and cooling down to 50 °C in Ar flow. Then, 10 vol % H_2 in Ar was injected until saturation at 50 °C and then purged with Ar until the baseline was stable, prior to carrying out TPD up to 600 °C at a heating rate of 10 °C/min. Ag_2O was taken as the standard material to correlate the peak areas to volume data.

3.4. Catalyst Test

Liquid-phase hydrogenation of MA was carried out over $M/CeO_{2-\delta}$ catalysts in a batch reactor at 210 °C and 5 MPa. The reduced catalysts (0.1 g) and MA (4.9 g) were put in an autoclave (100 mL) containing THF (40 mL) solvent and purged five times with nitrogen to remove air before pressurizing up to 4.0 MPa using hydrogen. The diffusional limitation including internal and external diffusion were ruled out by performing experiments varying the particles size of the catalyst (0.425–0.250 mm) and adjusting the string rate of 500 rpm. Simultaneously, the hydrogen pressure was raised up to and maintained at 5.0 MPa. The reaction effluents were analysed using a 7890A gas chromatograph (Agilent, Santa Clara, CA, USA) equipped with an SE-52 (30 m × 0.32 mm × 1.0 μm) capillary column and a flame ionization detector (FID). The programmed temperature from 100 °C–120 °C with a ramp of 5 °C/min was used to ensure complete separation of individual components in the effluents. The temperatures of the injector and detector were set at 260 °C and 190 °C, respectively.

MA conversion and yield of the product were calculated according to the following equations:

$$X_{MA}\ (\%) = (C_{SA} + C_{GBL})/(C_{MA} + C_{SA} + C_{GBL}) \times 100\% \quad (4)$$

$$S_{MA}\ (\%) = (C_{SA} + C_{GBL})/(C_{SA} + C_{GBL}) \times 100\% \quad (5)$$

$$Y_{SA}\ (\%) = C_{SA}/(C_{MA} + C_{SA} + C_{GBL}) \times 100\% \quad (6)$$

$$Y_{GBL}\ (\%) = C_{GBL}/(C_{MA} + C_{SA} + C_{GBL}) \times 100\% \quad (7)$$

where C_{MA}, C_{SA} and C_{GBL} represent the percent content of the reactant and products in the reaction effluent, respectively. X_{MA}, S_{SA}, Y_{SA} and Y_{GBL} represent the MA conversion, SA selectivity and the SA and GBL yields.

The turnover frequency (TOF) of the MA hydrogenation to SA (in the first 10 min) and the subsequent hydrogenation of SA to GBL (in the following 60 min) were calculated using the following formulae:

$$\mathrm{TOF_{MA\rightarrow SA}} = n(\mathrm{MA_{int.}}) \times \mathrm{X_{MA}}/(\mathrm{t} \times n(\mathrm{M_{surf.}})) \quad (8)$$

$$\mathrm{TOF_{SA-GBL}} = n(\mathrm{MA_{int.}}) \times \mathrm{Y_{GBL}}/(\mathrm{t} \times n(\mathrm{M_{surf.}})) \quad (9)$$

where $n(\mathrm{MA_{int.}})$ denotes the initial amount of MA in mol, $\mathrm{X_{MA}}$ the conversion of MA, $\mathrm{Y_{GBL}}$ the yield of GBL (%), t the reaction time (min) and $n(\mathrm{M_{surf.}})$ the surface metallic M atom number on the corresponding catalyst.

4. Conclusions

$Ni/CeO_{2-\delta}$, $Co/CeO_{2-\delta}$ and $Cu/CeO_{2-\delta}$ catalysts for maleic anhydride hydrogenation were prepared via a simple wet impregnation synthesis and well characterised applying XRD, TEM, Raman, TPR and TPD techniques, in order to unravel the dependence of the MAH performance over the redox properties and their M-$CeO_{2-\delta}$ interaction and, thus, guide the future design of robust and highly selective transition metal catalysts for MAH.

It was found that metal dispersion of $M/CeO_{2-\delta}$ catalysts declines as $Ni/CeO_{2-\delta}$ > $Co/CeO_{2-\delta}$ > $Cu/CeO_{2-\delta}$, in opposition to the order of metal crystallite sizes. The small metal crystallite sizes of the $M/CeO_{2-\delta}$ catalysts are found proportional to their oxide precursors, revealing that the strong MO_x-CeO_2 interaction plays a crucial role in governing the metal dispersion and particle sizes of the $M/CeO_{2-\delta}$ catalysts.

The O_{vac} concentrations in the $M/CeO_{2-\delta}$ catalysts are observed to be enhanced one magnitude relative to $CeO_{2-\delta}$, in the increasing sequence of $Cu/CeO_{2-\delta}$ > $Ni/CeO_{2-\delta}$ > $Co/CeO_{2-\delta}$ >> $CeO_{2-\delta}$. The increased O_{vac} concentration in $M/CeO_{2-\delta}$ is mainly due to the H_2 spillover from the metals to ceria, which favours the creation of O_{vac} in the ceria matrices. The H_2 reduction-induced metal exit from ceria matrices, sintering and O_{vac} is responsible for the increased crystallite size of the $CeO_{2-\delta}$ support.

The $CeO_{2-\delta}$ itself is evidenced an active support for SA generation since it shows notable activity in MAH to SA, yet is inert in SA hydrogenolysis to GBL. The metal loading greatly enhances the MAH activity and the SA selectivity on the $M/CeO_{2-\delta}$ catalysts. The apparent activity and turn over frequencies of MAH to SA ($\mathrm{TOF_{MA\rightarrow SA}}$) increase following the trend of $Ni/CeO_{2-\delta}$ > $Co/CeO_{2-\delta}$ > $Cu/CeO_{2-\delta}$ >> $CeO_{2-\delta}$. Among the examined catalysts, the $Ni/CeO_{2-\delta}$ displays the highest activity and selectivity to SA in the initial 40 min and the following SA hydrogenolysis to GBL. $\mathrm{TOF_{MA\rightarrow SA}}$ (61.7 $\mathrm{min^{-1}}$) on $Ni/CeO_{2-\delta}$ is twice- and five-times those on $Co/CeO_{2-\delta}$ ($\mathrm{TOF_{MA\rightarrow SA}}$ = 31.2 $\mathrm{min^{-1}}$) and $Cu/CeO_{2-\delta}$ ($\mathrm{TOF_{MA\rightarrow SA}}$ = 13.2 $\mathrm{min^{-1}}$), respectively. $Ni/CeO_{2-\delta}$ also possesses higher activity and selectivity than $Co/CeO_{2-\delta}$ in SA → GBL. The SA hydrogenolysis to GBL occurs on $Ni/CeO_{2-\delta}$ and $Co/CeO_{2-\delta}$ catalysts only when the conversion to SA completes, though no SA hydrogenolysis is observed on the $Cu/CeO_{2-\delta}$ and $CeO_{2-\delta}$ catalysts.

The MAH to SA on the $Ni/CeO_{2-\delta}$, $Co/CeO_{2-\delta}$ and $CeO_{2-\delta}$ catalysts follows the first order kinetic law, but $Cu/CeO_{2-\delta}$ displays a more complex kinetic mechanism. $CeO_{2-\delta}$ may catalyse MAH to SA and favours the MAH on $Ni/CeO_{2-\delta}$, though O_{vac} is not a dominant factor for the enhanced MAH performance, as shown by the facts that both $CeO_{2-\delta}$ and $Cu/CeO_{2-\delta}$ are inert in SA hydrogenolysis and the O_{vac}-richest $Cu/CeO_{2-\delta}$ is not robust in SA generation. The electronic configurations of the metals are supposed crucial for the activation of H_2, MA and SA in the MAH. Therefore, the distinct catalytic hydrogenation behaviour on the catalysts arises from the synergistic

contributions of the metal dispersion, O_{vac} concentration and the metal electronic configurations, which determine the activation of hydrogen and double bonds in MA and SA.

Supplementary Materials: The following are available online at www.mdpi.com/2073-4344/7/9/272/s1, Figure S1: The dependence of metal crystallite sizes on those of metal oxides in the $xNi/CeO_{2-\delta}$ catalysts (x represents the loading amount (wt %) of Ni in the $xNi/CeO_{2-\delta}$ catalysts).

Acknowledgments: This work was partially supported by the Natural Science Foundation of China (No. 21503124), the Key Coal Technologies R&D Program of Shanxi Province (No. MH2014-06), the Science and Technology Program of Shanxi Province (No. 20140321013-02) and the Royal Society International collaboration award. X.L. appreciates the Eustice studentship from Southampton University. We sincerely appreciate Dr Kevin Chung-che Huang (Optical Research Centre, University of Southampton) for his kind help in Raman characterization.

Author Contributions: The idea was conceived of by Y.Z. and Z.J. X.L. performed the experiments and drafted the paper under the supervision of Y.Z., Z.J. and M.H. L.Z. and Y.Z. helped to collect and analyse some characterization data. The manuscript was revised through the comments of all authors. All authors have given approval for the final version of the manuscript.

Conflicts of Interest: The authors declare no conflict of interest.

References

1. Liao, X.; Zhang, Y.; Hill, M.; Xia, X.; Zhao, Y.; Jiang, Z. Highly efficient Ni/CeO_2 catalyst for the liquid phase hydrogenation of maleic anhydride. *Appl. Catal. A* **2014**, *488*, 256–264. [CrossRef]
2. Bertone, M.E.; Meyer, C.I.; Regenhardt, S.A.; Sebastian, V.; Garetto, T.F.; Marchi, A.J. Highly selective conversion of maleic anhydride to γ-butyrolactone over Ni-supported catalysts prepared by precipitation–deposition method. *Appl. Catal. A Gen.* **2015**, *503*, 135–146. [CrossRef]
3. Meyer, C.I.; Regenhardt, S.A.; Marchi, A.J.; Garetto, T.F. Gas phase hydrogenation of maleic anhydride at low pressure over silica-supported cobalt and nickel catalysts. *Appl. Catal. A* **2012**, *417–418*, 59–65. [CrossRef]
4. Delhomme, C.; Weuster-Botz, D.; Kühn, F.E. Succinic acid from renewable resources as a C4 building-block chemical—A review of the catalytic possibilities in aqueous media. *Green Chem.* **2009**, *11*, 13–26. [CrossRef]
5. Castiglioni, G.; Vaccari, A.; Fierro, G.; Inversi, M.; Lojacono, M.; Minelli, G.; Pettiti, I.; Porta, P.; Gazzano, M. Structure and reactivity of copper-zinc-cadmium chromite catalysts. *Appl. Catal. A* **1995**, *123*, 123–144. [CrossRef]
6. Regenhardt, S.A.; Meyer, C.I.; Garetto, T.F.; Marchi, A.J. Selective gas phase hydrogenation of maleic anhydride over Ni-supported catalysts: Effect of support on the catalytic performance. *Appl. Catal. A* **2012**, *449*, 81–87. [CrossRef]
7. Castiglioni, G.L.; Ferrari, M.; Guercio, A.; Vaccari, A.; Lancia, R.; Fumagalli, C. Chromium-free catalysts for selective vapor phase hydrogenation of maleic anhydride to γ-butyrolactone. *Catal. Today* **1996**, *27*, 181–186. [CrossRef]
8. Zhang, D.; Yin, H.; Xue, J.; Ge, C.; Jiang, T.; Yu, L.; Shen, Y. Selective hydrogenation of maleic anhydride to tetrahydrofuran over Cu–Zn–M (M = Al, Ti, Zr) catalysts using ethanol as a solvent. *Ind. Eng. Chem. Res.* **2009**, *48*, 11220–11224. [CrossRef]
9. Meyer, C.I.; Marchi, A.J.; Monzon, A.; Garetto, T.F. Deactivation and regeneration of Cu/SiO_2 catalyst in the hydrogenation of maleic anhydride. Kinetic modeling. *Appl. Catal. A Gen.* **2009**, *367*, 122–129. [CrossRef]
10. Bertone, M.E.; Regenhardt, S.A.; Meyer, C.I.; Sebastian, V.; Garetto, T.F.; Marchi, A.J. Highly selective Cu-modified Ni/SiO_2–Al_2O_3 catalysts for the conversion of maleic anhydride to γ-butyrolactone in gas phase. *Top. Catal.* **2015**, *59*, 159–167. [CrossRef]
11. Li, J.; Qian, L.-P.; Hu, L.-Y.; Yue, B.; He, H.-Y. Low-temperature hydrogenation of maleic anhydride to succinic anhydride and γ-butyrolactone over pseudo-boehmite derived alumina supported metal (metal=Cu, Co and Ni) catalysts. *Chin. Chem. Lett.* **2016**, *27*, 1004–1008. [CrossRef]
12. Yu, Y.; Guo, Y.; Zhan, W.; Guo, Y.; Wang, Y.; Wang, Y.; Zhang, Z.; Lu, G. Gas-phase hydrogenation of maleic anhydride to γ-butyrolactone at atmospheric pressure over Cu–CeO_2–Al_2O_3 catalyst. *J. Mol. Catal. A Chem.* **2011**, *337*, 77–81. [CrossRef]
13. Lu, W.; Lu, G.; Guo, Y.; Guo, Y.; Wang, Y. Gas-phase hydrogenation of maleic anhydride to butyric acid over $Cu/TiO_2/\gamma$-Al_2O_3 catalyst promoted by Pd. *Catal. Commun.* **2003**, *4*, 177–181. [CrossRef]

14. Gao, C.-G.; Zhao, Y.-X.; Zhang, Y.; Liu, D.-S. Synthesis characterization and catalytic evaluation of $Ni/ZrO_2/SiO_2$ aerogels catalysts. *J. Sol-Gel Sci. Technol.* **2007**, *44*, 145–151. [CrossRef]
15. Zhang, D.; Yin, H.; Zhang, R.; Xue, J.; Jiang, T. Gas phase hydrogenation of maleic anhydride to γ-butyrolactone by cu–zn–ce catalyst in the presence of n-butanol. *Catal. Lett.* **2007**, *122*, 176–182. [CrossRef]
16. Zhang, R.; Yin, H.; Zhang, D.; Qi, L.; Lu, H.; Shen, Y.; Jiang, T. Gas phase hydrogenation of maleic anhydride to tetrahydrofuran by $Cu/ZnO/TiO_2$ catalysts in the presence of n-butanol. *Chem. Eng. J.* **2008**, *140*, 488–496. [CrossRef]
17. Torres, C.C.; Alderete, J.B.; Mella, C.; Pawelec, B. Maleic anhydride hydrogenation to succinic anhydride over mesoporous Ni/TiO_2 catalysts: Effects of Ni loading and temperature. *J. Mol. Catal. A Chem.* **2016**, *423*, 441–448. [CrossRef]
18. Bruix, A.; Rodriguez, J.A.; Ramirez, P.J.; Senanayake, S.D.; Evans, J.; Park, J.B.; Stacchiola, D.; Liu, P.; Hrbek, J.; Illas, F. A new type of strong metal-support interaction and the production of H_2 through the transformation of water on $Pt/CeO_2(111)$ and $Pt/CeO_x/TiO_2(110)$ catalysts. *J. Am. Chem. Soc.* **2012**, *134*, 8968–8974. [CrossRef] [PubMed]
19. Campbell, C.T. Catalyst-support interactions: Electronic perturbations. *Nat. Chem.* **2012**, *4*, 597–598. [CrossRef] [PubMed]
20. Farmer, J.A.; Campbell, C.T. Ceria maintains smaller metal catalyst particles by strong metal-support bonding. *Science* **2010**, *329*, 933–936. [CrossRef] [PubMed]
21. Carrasco, J.; Lopez-Duran, D.; Liu, Z.; Duchon, T.; Evans, J.; Senanayake, S.D.; Crumlin, E.J.; Matolin, V.; Rodriguez, J.A.; Ganduglia-Pirovano, M.V. In situ and theoretical studies for the dissociation of water on an active Ni/CeO_2 catalyst: Importance of strong metal-support interactions for the cleavage of O-H bonds. *Angew. Chem. Int. Ed. Engl.* **2015**, *54*, 3917–3921. [CrossRef] [PubMed]
22. Sakai, M.; Nagai, Y.; Aoki, Y.; Takahashi, N. Investigation into the catalytic reduction of NO_x at copper–ceria interface active sites. *Appl. Catal. A* **2016**, *510*, 57–63. [CrossRef]
23. Wang, F.; He, S.; Chen, H.; Wang, B.; Zheng, L.; Wei, M.; Evans, D.G.; Duan, X. Active site dependent reaction mechanism over Ru/CeO_2 catalyst toward CO_2 methanation. *J. Am. Chem. Soc.* **2016**, *138*, 6298–6305. [CrossRef] [PubMed]
24. Kehoe, A.B.; Scanlon, D.O.; Watson, G.W. Role of lattice distortions in the oxygen storage capacity of divalently doped CeO_2. *Chem. Mater.* **2011**, *23*, 4464–4468. [CrossRef]
25. Liu, Y.; Murata, K.; Inaba, M. Steam reforming of bio-ethanol to produce hydrogen over Co/CeO_2 catalysts derived from $Ce_{1-x}Co_xO_{2-y}$ precursors. *Catalysts* **2016**, *6*, 26. [CrossRef]
26. Cui, Y.; Dai, W.-L. Support morphology and crystal plane effect of Cu/CeO_2 nanomaterial on the physicochemical and catalytic properties for carbonate hydrogenation. *Catal. Sci. Technol.* **2016**, *6*, 7752–7762. [CrossRef]
27. Sohlberg, K.; Pantelides, S.T.; Pennycook, S.J. Interactions of hydrogen with CeO_2. *J. Am. Chem. Soc.* **2001**, *123*, 6609–6611. [CrossRef] [PubMed]
28. Shan, W.; Shen, W.; Li, C. Structural characteristics and redox behaviors of $Ce_{1-x}Cu_xO_y$ solid solutions. *Chem. Mater.* **2003**, *15*, 4761–4767. [CrossRef]
29. Tang, K.; Liu, W.; Li, J.; Guo, J.; Zhang, J.; Wang, S.; Niu, S.; Yang, Y. The effect of exposed facets of ceria to the nickel species in nickel-ceria catalysts and their performance in a NO + CO reaction. *ACS Appl. Mater. Interfaces* **2015**, *7*, 26839–26849. [CrossRef] [PubMed]
30. Greluk, M.; Rotko, M.; Machocki, A. Conversion of ethanol over Co/CeO_2 and $K\text{-}Co/CeO_2$ catalysts for hydrogen production. *Catal. Lett.* **2015**, *146*, 163–173. [CrossRef]
31. De Lima, S.M.; da Silva, A.M.; da Costa, L.O.O.; Graham, U.M.; Jacobs, G.; Davis, B.H.; Mattos, L.V.; Noronha, F.B. Study of catalyst deactivation and reaction mechanism of steam reforming, partial oxidation, and oxidative steam reforming of ethanol over Co/CeO_2 catalyst. *J. Catal.* **2009**, *268*, 268–281. [CrossRef]
32. Tang, X.; Zhang, B.; Li, Y.; Xu, Y.; Xin, Q.; Shen, W. Carbon monoxide oxidation over CuO/CeO_2 catalysts. *Catal. Today* **2004**, *93–95*, 191–198. [CrossRef]
33. Matte, L.P.; Kilian, A.S.; Luza, L.; Alves, M.C.M.; Morais, J.; Baptista, D.L.; Dupont, J.; Bernardi, F. Influence of the CeO_2 support on the reduction properties of Cu/CeO_2 and Ni/CeO_2 nanoparticles. *J. Phys. Chem. C* **2015**, *119*, 26459–26470. [CrossRef]
34. Spanier, J.E.; Robinson, R.D.; Zhang, F.; Chan, S.-W.; Herman, I.P. Size-dependent properties of CeO_{2-y} nanoparticles as studied by raman scattering. *Phys. Rev. B* **2001**, *64*, 245407. [CrossRef]

35. Wu, Z.; Li, M.; Howe, J.; Meyer, H.M.; Overbury, S.H. Probing defect sites on CeO_2 nanocrystals with well-defined surface planes by raman spectroscopy and O_2 adsorption. *Langmuir ACS J. Surf. Coll.* **2010**, *26*, 16595–16606. [CrossRef] [PubMed]
36. Liu, J.; Li, C.; Wang, F.; He, S.; Chen, H.; Zhao, Y.; Wei, M.; Evans, D.G.; Duan, X. Enhanced low-temperature activity of CO_2 methanation over highly-dispersed Ni/TiO_2 catalyst. *Catal. Sci. Technol.* **2013**, *3*, 2627. [CrossRef]
37. Znak, L.; Zieliński, J. Effects of support on hydrogen adsorption/desorption on nickel. *Appl. Catal. A* **2008**, *334*, 268–276. [CrossRef]
38. Hammer, B.; Nørskov, J.K. Electronic factors determining the reactivity of metal surfaces. *Surf. Sci.* **1995**, *343*, 211–220. [CrossRef]
39. Pallassana, V.; Neurock, M.; Coulston, G.W. Theoretical density functional analysis of maleic anhydride chemisorption on Pd(111), Re(0001), and bimetallic $Pd_{ML}/Re(0001)$ and $Pd_{ML}/Mo(110)$ pseudomorphic overlayers. *J. Phys. Chem. B* **1999**, *103*, 8973–8983. [CrossRef]
40. Zhang, S.; Li, J.; Xia, Z.; Wu, C.; Zhang, Z.; Ma, Y.; Qu, Y. Towards highly active Pd/CeO_2 for alkene hydrogenation by tuning Pd dispersion and surface properties of the catalysts. *Nanoscale* **2017**, *9*, 3140–3149. [CrossRef] [PubMed]
41. Wu, X.P.; Gong, X.Q.; Lu, G. Role of oxygen vacancies in the surface evolution of H at $CeO_2(111)$: A charge modification effect. *Phys. Chem. Chem. Phys.* **2015**, *17*, 3544–3549. [CrossRef] [PubMed]
42. Pallassana, V.; Neurock, M. First-principles periodic density functional study of the hydrogenation of maleic anhydride to succinic anhydride over palladium(111). *J. Phys. Chem. B* **2000**, *104*, 9449–9459. [CrossRef]
43. Pallassana, V.; Neurock, M.; Coulston, G. Towards understanding the mechanism for the selective hydrogenation of maleic anhydride to tetrahydrofuran over palladium. *Catal. Today* **1999**, *50*, 589–601. [CrossRef]
44. Claus, P.; Brückner, A.; Mohr, C.; Hofmeister, H. Supported gold nanoparticles from quantum dot to mesoscopic size scale: Effect of electronic and structural properties on catalytic hydrogenation of conjugated functional groups. *J. Am. Chem. Soc.* **2000**, *122*, 11430–11439. [CrossRef]
45. Vile, G.; Bridier, B.; Wichert, J.; Perez-Ramirez, J. Ceria in hydrogenation catalysis: High selectivity in the conversion of alkynes to olefins. *Angew. Chem. Int. Ed. Engl.* **2012**, *51*, 8620–8623. [CrossRef] [PubMed]
46. Ponec, V. On the role of promoters in hydrogenations on metals; α,β-unsaturated aldehydes and ketones. *Appl. Catal. A* **1997**, *149*, 27–48. [CrossRef]
47. Mäki-Arvela, P.; Hájek, J.; Salmi, T.; Murzin, D.Y. Chemoselective hydrogenation of carbonyl compounds over heterogeneous catalysts. *Appl. Catal. A* **2005**, *292*, 1–49. [CrossRef]
48. Dandekar, A.; Vannice, M.A. Crotonaldehyde hydrogenation on Pt/TiO_2 and Ni/TiO_2 SMSI catalysts. *J. Catal.* **1999**, *183*, 344–354. [CrossRef]
49. Herrmann, U.; Emig, G. Kinetics and mechanism in the liquid-phase hydrogenation of maleic anhydride and intermediates. *Chem. Eng. Technol.* **1998**, *21*, 285–295. [CrossRef]
50. Gil Girol, S.; Strunskus, T.; Muhler, M.; Wöll, C. Reactivity of ZnO surfaces toward maleic anhydride. *J. Phys. Chem. B* **2004**, *108*, 13736–13745. [CrossRef]